HHS Public Access

Author manuscript

Biomed Mater. Author manuscript; available in PMC 2022 January 15.

Published in final edited form as:

Biomed Mater. ; 16(3): . doi:10.1088/1748-605X/abc107.

Fabrication and characterization of a thick, viable bi-layered stem cell-derived surrogate for future myocardial tissue regeneration

Danielle Pretorius, **Asher M Kahn-Krell**, **Wesley C LaBarge**, **Xi Lou**, **Ramaswamy Kannappan**, **Andrew E Pollard**, **Vladimir G Fast**, **Joel L Berry**, **Alan W Eberhardt**, **Jianyi Zhang**

Department of Biomedical Engineering, School of Medicine and School of Engineering, University of Alabama at Birmingham, Birmingham, Alabama 35294, United States of America

Abstract

Cardiac tissue surrogates show promise for restoring mechanical and electrical function in infarcted left ventricular (LV) myocardium. For these cardiac surrogates to be useful *in vivo*, they are required to support synchronous and forceful contraction over the infarcted region. These design requirements necessitate a thickness sufficient to produce a useful contractile force, an area large enough to cover an infarcted region, and prevascularization to overcome diffusion limitations. Attempts to meet these requirements have been hampered by diffusion limits of oxygen and nutrients (100–200 μm) leading to necrotic regions. This study demonstrates a novel layer-by-layer (LbL) fabrication method used to produce tissue surrogates that meet these requirements and mimic normal myocardium in form and function. Thick (1.5–2 mm) LbL cardiac tissues created from human induced pluripotent stem cell-derived cardiomyocytes and endothelial cells were assessed, *in vitro*, over a 4-week period for viability (<5.6 ± 1.4% nectrotic cells), cell morphology, viscoelastic properties and functionality. Viscoelastic properties of the cardiac surrogates were determined via stress relaxation response modeling and compared to native murine LV tissue. Viscoelastic characterization showed that the generalized Maxwell model of order 4 described the samples well ($0.7 < R^2 < 0.98$). Functional performance assessment showed enhanced t-tubule network development, gap junction communication as well as conduction velocity (16.9 ± 2.3 cm s^{-1}). These results demonstrate that LbL fabrication can be utilized successfully in creating complex, functional cardiac surrogates for potential therapeutic applications.

Keywords

layer-by-layer; tissue engineering; stem cell; viscoelasticity; vascularization; cardiac regeneration

jayzhang@uab.edu .

Supplementary material for this article is available https://doi.org/10.1088/1748-605X/abc107

1. Introduction

Cardiac tissue engineering strategies focusing on recellularization and functional restoration after acute myocardial infarction (AMI) have shown promise to improve the clinical outcomes for patients [1–3]. Clinically, AMI is associated with contractile cell-loss, particularly in the left ventricle (LV), resulting in increased risks of arrhythmia and postinfarction LV remodeling. Cell therapies using the products of human induced pluripotent stem cells (hiPSCs) have been examined, pre-clinically [4], as a viable therapeutic option with their ability to produce patient-specific cardiac cells [5, 6]. In light of these results, the search continues for an effective method of restoring function of the AMI damaged heart, which is necessary for a successful therapeutic application. Furthermore, mechanical stabilization of the damaged region is also required to prevent excessive ventricular dilatation [7, 8].

A healthy myocardium maintains its structure and function under billions of pumping cycles. Much is known about the mechanics of myocardium as a hyperviscoelastic tissue undergoing large deformations during filling and pumping [9–11] but the mechanics of tissue surrogates is highly understudied. At present, there is a gap in knowledge related to how tissue surrogates function in both the short- as well as the long-term as true functional support structures to infarcted hearts. In addition, passive mechanical mismatch in compliance has the potential to induce further damage via maladaptive remodeling. Wang *et al* [12] found that scaffolds with mismatched stiffness, compared to the native myocardium, were unable to reduce infarcted myocardial wall stress. Furthermore mismatched scaffold flexibility adversely affected active mechanical properties, specifically failing to mimic active myocardial contraction and expansion. Engineered surrogates that closely capture the mechanical properties of the host myocardium have been shown to support the direction and propagation of progenitor cells associated with tissue regeneration [13, 14]. In addition, viscoelastic parameters, like creep and stress relaxation, that describe the time and rate dependency of the mechanical response to deformation have been shown to be vital for a tissue-engineered replacements to be successful [15].

One promising fabrication method is the layer-by-layer (LbL) approach in which sequential layers of material are deposited individually. Many LbL fabrication methods have been developed over the past five decades [16–18], making notable contributions to various fields, including the pharmaceutical and cosmetic industries [19, 20]. In a functional myocardium, cardiomyocytes (CMs) are typically adjacent to one another as opposed next to the smooth muscle cells, fibroblasts (FBs) or endothelial cells (ECs). The mixing of cardiac cells in previous engineered cardiac tissue, likely prevented the hiPSC-CMs from coalescing into a fully interconnected contractile apparatus and may partially explain why force-generation measurements remained lower than in native heart tissue [21]. LbL fabrication allows for a high degree of control over physicochemical properties, including construct architecture, permeability, and Young's (elastic) modulus [22–26]. When engineering tissue like the myocardium, this technique has the potential to enhance construct performance, as it allows for the sequential deposition of specialized cells as opposed to depositing large volumes of co-cultured cells. This is especially important for functional aspects such as contractile function and electromechanical connectivity for example [27]. Unfortunately,

current production of thick implantable engineered tissue is hampered by the fact that 3D structures lacking adequate vascularization generally become necrotic within 100–200 μm of the boundary regions [28–30]. EC presence in the myocardium is not limited to providing vascularization but is vital to adult CM function, including CM organization and contractile force generation [31–37]. Numerous strategies have aimed to optimize vascularization in engineered tissue using variations of LbL techniques [38–41], yet due to oxygen- and nutrient limitations [42, 43] cardiac surrogates thicker than 250 μm are rarely seen without significant degrees of necrosis. These previous LbL approaches have, however, allowed for the production of, albeit thin, native tissue-like metabolically active structures that possessed blood vessels. Studies on temperature-responsive (poly(N-isopropylacrylamide)) PIPAAm-sheets seeded with CMs showed that the layers were not only capable of being detached from their 2D culturing environment and fusing, but post-fusion, were able to conduct electrical signals synchronously [44]. These synchronous conduction capabilities can be attributed to factors like cellular alignment and coupling, along with the maturation of calcium-handling machinery like t-tubule networks as expressed by markers for junctophilin-2 (JP2) and ryanodine receptor (RyR) [45, 46]. In total, the current LbL techniques for fabricating cardiac surrogates have not yielded a clinically viable alternative.

In the present study, we aimed at developing a thick, viable cardiac tissue surrogate from hiPSC-derived cells. The cardiac surrogates were characterized at various time points in order to inform future decisions, including optimal implantation time post-fabrication as well as material composition. Characterization included (1) histology and immunostainig to analyze the cellular and structural morphology, (2) immunostaining to quantify viability, (3) immunostaining of 2D and 3D structures to analyze cell migration and vascularization, (4) stress relaxation tests and subsequent model fitting of the responses to determine the viscoelastic properties, (5) immunostaining and quantification of ECM remodeling and how it is related to the viscoelastic properties of the cardiac surrogates, (6) electron microscopy to examine the ultrastructure of the tissue and (7) optical mapping to determine the action potential and conduction velocity spectra to assess functionality. It was hypothesized that utilizing a modular fabrication approach, such as LbL deposition, would not only allow for the production of thicker tissues but also increase their robustness in terms of long-term culturability.

2. Materials and methods

2.1. Cell culture and characterization

hiPSCs were reprogrammed from human cardiac FBs, and subsequently differentiated into iCMs, as previously reported [4, 47, 48]. Generally, spontaneous contractions were observed in the iCM cultures between days 7 and 10 after the differentiation protocol commenced, with beating numbers increasing up to day 12. Metabolic purification of iCMs via glucose deprivation (RPMI 1640 without glucose, supplemented with sodium DL-lactate and $B27^{+}$, Gibco) for 3–6 d, initiated at day 11, allowed for a population of iCMs that was at least 95% cTnT positive. hiPSCs were maintained at optimal conditions, as previously described [49], on six-well plates coated with Matrigel (Corning), using mTeSR 1 maintenance media (STEMCell Technologies, Canada). hiPSC-ECs (iECs) were differentiated as described

previously [21, 50, 51]. Briefly, undifferentiated hiPSCs were seeded into a 0.5 mL fibrin scaffold and treated with CHIR99021 and U46619 in EBM2 medium (Lonza, USA) supplemented with $B27^-$ for 24 h. The medium was replaced with EBM2 supplemented with $B27^-$, vascular endothelial growth factor (VEGF), erythropoietin, and transforming growth factor β1, and then cultured for 96 h with a media change halfway through. Finally, the scaffold was released and cultured in EGM2-MV medium (Lonza, USA) supplemented with $B27^+$, VEGF, SB-431542, with media changes every two days. hiPSC-ECs were purified and enriched by collecting cells positive for CD31 using fluorescence-activated cell sorting device (FACSAria II). Antibodies used for selection along with dilutions are listed supplemental table 1. See supplemental figure 1 (stacks.iop.org/BMM/16/035007/mmedia) for cell characterization and supplemental figure 2 for the proliferation assay performed in to prove the lack of tumorigenic properties of the iCMs utilized.

2.2. Fibrin matrix composition

The supporting fibrin matrix (per milliliter) used for each alternating layer of the cardiac tissue fabrication consisted of the following components as was defined previously [21]: 0.12 mL fibrinogen (25 mg mL^{-1}, Sigma-Aldrich, CAS#9001–32–5), 0.02 mL Matrigel (Corning, #356 235), 0.56 mL of HEPES (20 mM, pH 7.4, Corning), 0.001 mL $CaCl_2$ (2 M), 0.3 mL DMEM (Gibco, High glucose, #11 965–118), 0.006 mL thrombin (80 U mL^{-1}, MP Biomedicals).

2.3. Polydimethylsiloxane (PDMS) stilts

PDMS stilts were fabricated by mixing PDMS (Dow Corning Sylgard 184 Silicone, Product #2 065 622) in a 10:1 elastomer:curing agent ratio and poured into a 100 mm diameter Pyrex Petri dish (Corning, #3 160 102). These were cured at 75 °C for 2 h in an oven, after which custom stilts of 10 mm $\times$ 5 mm (2.5 mm thick) were cut. All PDMS structures were autoclaved prior to use in tissue fabrication.

2.4. Optimized tissue surrogate fabrication

Following cell differentiation, cardiac tissue fabrication commenced (figure 1). Petri dishes (BioLite Cell Culture Treated Dishes, Thermo Scientific) were coated with a 5% pluronic F-68 solution (Gibco, #24 040 032) and incubated at 4 °C overnight. The pluronic solution was removed, and a sterile polycarbonate frame (internal area: 1 $\times$ 2 cm^2) was attached with a 2% agarose solution. Note that the frames were modified with channels to allow for maximal media contact following tissue fabrication. iCMs were dissociated (STEMdiff Cardiomyocyte Dissociation Medium, STEMCell) and mixed with the fibrin matrix at a concentration of 10 $\times 10^6$ cells mL^{-1}. Note that the deposition of the iCM layer denotes ‘D0’ for the remainder of the fabrication process. 400 µl of this solution was quickly deposited into each mold to produce the first layer. Following complete polymerization, the culture medium was added (STEMdiff Cardiomyocyte Support Medium, 2 mg mL^{-1} ε-aminocaproic acid) and incubated at 37 °C (5% CO_2) for 2 d. The next layer, comprised of iECs, was made in a similar fashion, with the following exceptions: iECs were dissociated using trypsin (0.25% trypsin, 0.1% EDTA, Corning, #25 053 CI) and then mixed with the fibrin matrix at a concentration of 10 $\times 10^6$ cells mL^{-1}. 200 µl of this solution was quickly deposited into each mold, yielding a 2:1 ratio of iCMs:iECs [21]. Fresh culture

medium (10% fetal bovine serum, 2% $B27^+$, and 2 mg mL^{-1} ε-aminocaproic acid, 10 μM ROCK inhibitor in DMEM) was added, following layer polymerization. After 24 h, the frame containing the cardiac tissue surrogate was lifted off of the dish surface and placed on top of custom-cut PDMS stilts, allowing for the tissue to be fully suspended in fresh culture media (2% fetal bovine serum, 2% $B27^+$, and 2 mg mL^{-1} ε-aminocaproic acid in DMEM). Incubation continued for the desired period of time (1–4 weeks in total), with media replacement once per week.

2.5. Tissue preservation

Samples were fixed in 4% formaldehyde (Pierce, Thermo Scientific, #28 906) for 1 h prior to embedding in either optimal cutting temperature compound (OCT compound, Fisher Health Care, USA) or paraffin for histological analysis (10 μm sections). Whole-mount samples were stored in PBS until staining.

2.6. Histochemistry

Deparaffinized and rehydrated sections were stained in hematoxylin solution (Mayer's, Merck, 3 min) then working eosin Y solution (2 min). Following dehydration sampled were mounted in Permount and imaged with a bright field microscope (Olympus IX83 epifluorescent microscope).

2.7. Immunohistochemistry

OCT embedded sections were blocked and permeabilized for 30 min in 10% donkey serum, 3% BSA, and 0.05% Triton-X. Primary antibodies were incubated for 1 h at room temperature (supplementary table 1). Following PBS wash (3 × 5 min), secondary antibodies labeled with fluorescent tags and 4′, 6-diamidino-2-phenylindole (DAPI, 100 ng mL^{-1}) were added for 1 h at room temperature (supplementary table 1). Sections were mounted in VECTASHIELD Antifade Mounting Medium and visualized by confocal laser scanning (Olympus FV3000 confocal microscope).

2.8. Whole-mount staining

Fixed whole-mount samples were blocked and permeabilized in 10% donkey serum, 10% Tween-20, 3% BSA, 0.05% Triton-X, and 0.2% sodium azide in PBS overnight at 4 °C. Primary antibodies were incubated overnight at 4 °C (supplementary table 1). Samples were washed in PBST (3 × 10 min) then fluorescently labeled secondary antibodies were added overnight at 4 °C with the addition of DAPI. Following washing, tissue was cleared according to the previously described protocol [52] with 3 h incubation in Ce3D clearing agent. Whole-mount constructs were transferred to an Ibidi μ-Slide (#80 286), covered with VECTASHIELD Antifade Mounting Medium, and visualized by confocal laser scanning.

2.9. Determination of structure viscoelastic properties

All sample specimens, including PDMS, fresh murine heart tissue and cardiac tissue surrogates were treated with the same procedure described here. Specimen size measurements (surface area, A) used in the determination of the stress from the forces measured ($\sigma = F/A$) were determined with a digital caliper (Mitutoyo 500–196–30,

Digimatic). Stress relaxation responses, stress *(σ)* vs. time *(t)*, were characterized using a generalized Maxwell model [53] of order 4 (figure 2(c)) in MATLAB (MathWorks, R2018, see supplemental information for the code). All specimens were transported from the incubator or sacrificed animal in chilled PBS and tested immediately. Stress relaxation testing in compression [54] was done using a Low Force Testbench (TA Instruments, New Castle, DE), where a 10% strain (ε) was applied and held for 4 min on each sample. Samples were strained (ε) at 10% by varying the applied deformation with thickness. Force (F) was measured with a 250 g load cell (figures 2(a), (b)).

The generalized Maxwell model was defined using the following equations, where E_i and η_i represent the modulus and viscosity of the i^{th} elements, and σ the measured stress:

$$\begin{aligned}\mathbf{M}odel:\sigma(\mathbf{t}) &= \varepsilon\mathbf{E}_0 + \varepsilon\mathbf{E}_1\left(\mathbf{e}^{-\frac{\mathrm{E}_1}{\eta_1}t}\right) + \varepsilon\mathbf{E}_2\left(\mathrm{e}^{-\frac{\mathrm{E}_2}{\eta_2}t}\right) \\ &+ \varepsilon\mathbf{E}_3\left(\mathrm{e}^{-\frac{\mathrm{E}_3}{\eta_3}\mathrm{t}}\right) + \varepsilon\mathbf{E}_4\left(\mathrm{e}^{-\frac{\mathrm{E}_4}{\eta_4}\mathrm{t}}\right)\end{aligned} \tag{1}$$

For each curve fit, the instantaneous modulus could be determined by the summation of each elastic modulus term ($t = 0$), whereas the equilibrium modulus was determined at $t \to \infty$ where $E_0 = \sigma/\varepsilon$. Viscosity was determined as the summation of each viscosity element (η_i).

$$\begin{aligned}&\textbf{Instantaneous Young}'\textbf{ smodulus }(\textbf{Pa}) = \mathbf{E}_0 + \mathbf{E}_1 + \\ &\mathbf{E}_2 + \mathbf{E}_3 + \mathbf{E}_4\end{aligned} \tag{2}$$

$$\textbf{Equilibrium Young}'\textbf{smodulus }(\textbf{Pa}) = \mathrm{E}_0 \tag{3}$$

$$\mathbf{V}iscosity\,(\mathbf{Pa}\cdot\mathrm{s}) = \eta_1 + \eta_2 + \eta_3 + \eta_4 \tag{4}$$

Prior to performing tests on the engineered tissue samples, the validity of this method was tested using PDMS of different crosslinking densities. Moduli and viscosity obtained from these validation experiments were used to confirm the goodness-of-fit for the Maxwell model of order 4 (figure 2(d)). The generalized Maxwell model of order 4 allowed for a good fit to the experimentally obtained data ($R^2 > 0.98$)

2.10. Animal studies: murine heart samples

Studies were performed using healthy murine hearts as a control sample in viscoelastic testing for cardiac tissue surrogates that were generated during this study. All animal procedures were performed in accordance with the guidelines for animal experimentation set forth and approved by Institutional Animal Care and Use Committee (IACUC, APN 20216), School of Engineering, University of Alabama at Birmingham; and conformed to the Guidelines for the Care and Use of Laboratory Animals published by the US National Institutes of Health (2011). Control tissue samples from SCID mouse LVs were obtained

after perfusion with saline and arrested in diastole by injection with 25 mM potassium chloride. Animals were gender-randomized.

2.11. Transmission electron microscope (TEM) imaging

Ultrastructural analysis of the thick cardiac tissue surrogates was done via TEM imaging. After culturing for the required amount of time (1–4 weeks), the tissue surrogates were fixed in a 2.5% glutaraldehyde solution for 1 h at 4 °C prior to being delivered to the UAB High-Resolution Imaging Facility for further processing. Sample blocks were sectioned using a diamond knife for clean and even sections. Samples were mounted and viewed using a Tecnai Spirit T12 TEM. Images were collected for analysis at each time point of interest (1 week, 2 weeks, and 4 weeks of tissue culture).

2.12. Four-electrode microimpedance spectra (4EMS)

To assess intercellular coupling in the tissue surrogates, we used systems of very small and closely spaced electrical sensors custom-fabricated into linear arrays that are integrated with adjacent instrumentation to provide low-amplitude stimulation current to the interstitial compartment of 15 preparations. Within each array, alternating current stimuli were delivered between the outer pair of electrodes at frequencies of 10 Hz to 4000 Hz as described previously [21, 55, 56]. Each stimulus established a 3D interstitial potential field that was then sensed as a voltage difference between sensors that formed an inner pair of electrodes that in turn allowed the identification of a microscopic composite impedance that included both real (tissue resistivity) and imaginary (tissue reactivity) components. At relatively low frequencies, supplied current remains primarily interstitial, and as a consequence, the current-to-voltage ratio provides information regarding the strength of interstitial electrical coupling. As frequency increases, supplied current shunts to the intracellular compartment via membrane capacitance and intracellular coupling strength becomes essential in assessing the response. Tissue resistivity and reactivity were identified during four sequential acquisition intervals in each preparation.

2.13. Optical mapping

To assess action potential duration, conduction velocity, and minimum pacing cycle length, LbL tissue surrogates were stained with a voltage-sensitive dye RH-237 (2.5 μM) for 10 min, transferred to a perfusion chamber mounted on an inverted microscope (scope details). Samples were perfused with Hank's balanced salt solution (HBSS) at approximately 37 °C. Sample pacing/stimulation was done with a bipolar electrode consisting of a glass pipette filled with HBSS and a silver wire coiled around its tip. The electrode tip was positioned at the sample's edge using a micromanipulator. Rectangular stimulation pulses were used, with a duration of 2 ms and current strength 1.5 times the excitation threshold. Fluorescence was excited with a 200-W Hg/Xe arc lamp and recorded with a 16 × 16 photodiode array (Hamamatsu) at a spatial resolution of 110 μm per diode as previously described [57]. Excitation light was filtered at 532–587 nm, and emitted fluorescent light was filtered at >650 nm. To eliminate motion artifacts caused by the sample's spontaneous contractions, the perfusion solution was supplemented with 5 μM of blebbistatin. Isochronal maps of the activation spread were constructed from activation times measured at 50% of the maximum action potential amplitude. Conduction velocity was calculated at each recording site from

local activation times and averaged across the whole mapping area. Action potential duration was measured at 50% and 80% of signal recovery (APD_{50}) and (APD_{80}), respectively.

2.14. Image analyses

All image quantification analyses were performed with ImageJ. Where indicated, arbitrary units are representative of a pixel count and intensity for each sample.

2.15. Statistical analyses

For statistical analysis, data are shown in the form mean ± SEM. Significance was chosen as $p < 0.05$. This was determined using either Student's t-test or ANOVA where applicable. One sample Wilcoxon tests ($\alpha = 0.05$) were used in the viscoelastic statistical analyses of between cardiac tissue surrogates ($n = 3$) and native murine LV tissue ($n = 5$). These analyses were performed utilizing GraphPad Prism8 data analysis software package.

3. Results

3.1. LbL fabrication produces thick, synchronously beating, fused tissue surrogates

Tissue surrogates produced with the optimized method described in figure 1 yielded structures of 1.73 ± 0.075 mm in thickness after 1 week in culture (figure 3(a)). Following the first 24 h post-iCM layer deposition (on D1), the beating-rate (per min) of each tissue surrogate was determined (figure 3(b)). This yielded a rate of 74 ± 8.4 beats min^{-1} (bpm). On the second day, the beat-rate lowered significantly ($p = 0.01$) to 63 ± 5.8 bpm. After iEC layer addition on D3 and an additional 3 d of culture (D6), the beating-rate on the sixth day had decreased further to 29 ± 4.1 bpm ($p = 0.0008$). Whether this significant decrease in bpm is due to paracrine signaling from the iECs or whether the internal cardiac pacemaker system become somewhat quiescent, remains to be seen.

Alterations in ECM composition between weeks 1 and 4 were observed via H&E staining (figures 3(c)–(h)). Histology suggests increases in structural ECM components such as collagen (increased intensity as well as the distribution of eosinophilic staining, figures 3(c)–(h). With increased culture time, compaction of the structures became more apparent (figure 3(f)), and structures, although initially somewhat disorganized, resembled *in vivo* muscle. Structure coupling was confirmed by not only the synchronous macroscopic beating of the tissue surrogates (figure 3(b)) but also through the fusion of the two layers as visualized on H&E sections. Another observation was the iEC migration out of their originally deposited layer into the resident iCM layer as is clear from the somewhat acellular appearance of the top layer of the tissue surrogate (figures 3(c)–(h)), Cell migration from the iEC later into the iCM resulted in a localized elevated concentration of iECs near the layer-fusion site, and was primarily evident during the initial culture stages (after 1 week, figures 3(c)–(e)) as opposed to later culture stages (week 4, figures 3(f)–(h)). Due to the difficulty in distinguishing between the different cells and their distribution throughout the structure based on H&E alone, further specific immunofluorescent staining was completed and quantified (figure 5). The effect of this migration on the viability of the cardiac surrogates was determined via immunofluorescent staining and subsequently quantified. It should be noted that structures visualized here via H&E staining appear thinner than those

preserved in OCT. This difference in overall tissue thickness can be attributed to the multiple dehydration-related steps required during the H&E processing of the hydrogel structures leading to decreased preservation of the original architecture.

3.2. LbL fabrication yields highly viable tissue

The viability of the tissue was determined with pMLKL staining (figure 4), which specifically stains for cell necroptosis [58] and is associated with inflammatory markers [59]. The pMLKL-positive cells were quantified as a percentage (%) of the total number of cells present (i.e. normalized to the DAPI staining). No significant differences were found in the degree of necrotic staining for any of the time points analyzed. The necrotic staining was quantified (figure 4(c)) as 4.5 $\pm$ 2.3% after 1 week, 4.3 $\pm$ 1.1% after 2 weeks, and 5.6 $\pm$ 1.4% after 4 weeks in culture (see supplemental figure 3 for staining at week 4). These values were comparable with the ~4% pMLKL positive staining obtained by Gao *et al* previously for their large tri-lineage iPSC-derived thick (1.25 mm) cardiac muscle patches after 1 week in culture [21].

3.3. Cell migration and tissue vascularization

Imaging of the fluorescently stained sections (figure 5) showed iEC migration into the iCM region of the dual-layered tissue surrogates. Evidence of migration was initially seen after day 5 and continued throughout the culture period. This migration process continued over the 4 weeks of culture, with clear integration into the iCM layer observed from the 2D sections by the 4th week (figure 5(a)). In order to confirm vasculature formation as well as establish a timeline for the formation process, whole-mount staining was employed. Staining of samples after 2 weeks of culture (figure 5(c)) showed branching vascular networks. Whole-mount staining further confirmed the observations regarding iEC integration and elucidated that iCM orientation was random and did not yet present with the degree of cell alignment seen in native myocardial tissue (figure 5(c)). Clear delineation of cell distribution can be seen in supplemental figure 4. Quantification of each cell type at weeks 1, 2 and 4, respectively, showed that the amount of CD31 expression relative to cTnT expression remained stable over the 4 week period with no statistically significant differences between the expression ratios at each time point ($n = 3$, supplemental figure 4(c)). Furthermore, no statistically significant differences between the cTnT expression relative to the DAPI expression was noted either ($n = 3$, supplemental figure 4(d)).

3.4. Use of the viscoelastic model in compression mode

Engineered tissue modeling over the 4 weeks yielded excellent fits to the experimentally obtained results, as $R^2 > 0.7$ for all samples from weeks 1 and 2 respectively, while $R^2 > 0.88$ for samples from week 4 (figure 6(a)). Instantaneous moduli of 4.72 $\pm$ 0.84 kPa, 5.82 $\pm$ 0.47 kPa, and 4.85 $\pm$ 0.16 kPa were measured for week 1, week 2, and week 4 samples, respectively (figure 6(b)). The standard deviation in the samples decreased as the culture time increased from 1 week to 2 weeks to 4 weeks. Viscosity modeling yielded values of $8.03 \times 10^4 \pm 2.42\times10^3$ Pa•s, $3.35 \times 10^4 \pm 6.31\times10^3$ Pa•s, and $6.70 \times 10^4 \pm 2.14\times10^4$ Pa•s respectively. Tissue surrogate viscoelastic properties ($n = 3$ for each group) were compared to those of healthy LV tissue from SCID mice ($n = 5$). Mouse LV tissue instantaneous modulus was measured at 6.43 $\pm$ 1.13 kPa, while viscosity was $2.00 \times 10^5 \pm$

8.32×10^4 Pa•s. Equilibrium moduli of 1.08 ± 0.31 kPa, 1.31 ± 0.37 kPa, and 0.40 ± 0.10 kPa were obtained for week 1, week 2, and week 4 samples, respectively (figure 6(c)). The equilibrium modulus for the control mouse LV samples was observed at 2.81 ± 0.48 kPa. Non-parametric tests (one sample Wilcoxon) showed that there were no statistically significant differences between the viscoelastic properties of the cardiac tissue surrogate and the healthy murine LV tissue ($\alpha = 0.05$), even with the differences in properties noted for the tissue surrogates at different time points.

3.5. Dynamic ECM evolution

During the 4-week culturing period, the ECM underwent multiple phases of remodeling. The degree to which this very dynamic process occurs was monitored and quantified *in vitro* through analysis of individual matrix component degradation and deposition. For ECM analyses, three samples were analyzed at each time point, with at least five images per matrix component. Since the fibrin used in the matrix fabrication consisted of both bovine thrombin and fibrinogen, an antibody targeting a bovine specific epitope was used in its analysis. An antibody with a fibrinogen β-chain that matched the β-chain section of the fibrinogen used to fabricate the fibrin matrix was used to stain and analyze the evolution of fibrin over 4 weeks in culture (figure 7(a)). Analysis showed discernable degradation of the fibrin matrix over this period. Since the engineered tissue remained structurally intact and previous research has shown that ECM remodeling occurs during iCM culturing [60, 61], samples were analyzed for additional ECM components, including collagen 1 (Col1), collagen 3 (Col3), collagen 4 (Col4), laminin (Lam) and fibronectin (FN) (figure 7(b)). Quantification showed a nearly three-fold increase in collagen one production from weeks 1–4. A general trend was observed in basal membrane component production, i.e. the relative amounts of both collagen four, as well as laminin, decreased from week 1 to week 2, to week 4. The variations in structural ECM components, like collagen 1, affect the overall stiffness of the tissue surrogates, whereas dense basement membrane components, including laminin and collagen 4, play more of a role in viscous properties [62–64]. The decreasing viscosity of the tissue surrogates (figure 6(b)) is likely linked to the reduction in basement membrane ECM components. Furthermore, week 2 saw a notable increase for fibronectin, which is highly expressed in the heart during early stages of embryogenesis and has also been shown to be vital in the vasculogenesis process [65]. The enhanced expression of fibronectin noted after 2 weeks in culture may be linked to the formation of the branched vessel-like structures noted in figure 5(c). In addition to altering viscosity properties of the structure, collagen 4 likely has another functional role, specifically that of an anti-angiogenic signaling cue [66, 67]. The statistically significant increase in collagen 4 in week 2 coincides with an even more notable statistically significant increase in fibronectin expression (figure 7(b)). This phenomenon can most likely be attributed to an ‘on-off ‘ switch regulating the vessel formation process occurring in the tissue surrogate.

3.6. Ultrastructure development is suggestive of tissue maturation

Alterations noted in the ECM via H&E and immuno-fluorescent staining (figures 3(c)–(h)) were also confirmed via TEM (figure 8). As culture-time increased from 1 to 4 weeks (figures 8(a) vs (c) vs (e), there was an increase in the number of gap junctions (GJ) observed between the cells (figure 8(d)). Increases in the number of GJ (see supplemental

figure 5 for immunofluorescent staining of connexin 43 as well as its quantification), along with the statistically significant increase in sarcomere length (distance between z-bands) from 1.53 ± 0.02–1.68 ± 0.12 μm between weeks 1 and 2, with a further increase to 1.70 ± 0.02 μm at week 4 (figure 8(g)) suggest that the fabrication method along with the extended culturing promote a degree of functional maturation [68]. These sarcomere lengths are physiologically relevant and compare with those observed in both neonatal rats and sheep (1.5–1.9 μm) [69, 70].

3.7. Functional performance of bi-layered tissue surrogates

Functional performance was assessed by t-tubule formation, intracellular GJ formation (4EMS) as well as optical mapping to determine conduction velocities through the tissue. All mapping of surrogates was performed after 1 week in culture. Staining and subsequent quantification of the tissue surrogates for both JP2 (figure 9(a), supplemental figure 6) and RyR (figure 9(b), supplemental figure 6) expression suggested that there was a significant increase in the number of t-tubules formed between the first and fourth week of tissue culture. Resistivity–reactivity spectra (figure 9(c)) compared favorably with spectra from our earlier report with rabbit LV myocardium [55], supporting GJ intracellular communication developed in these cardiac tissue surrogates to an extent similar to that in native myocardium. The heatmap generated from optical mapping (figure 9(d)) shows a lack of arrhythmogenicity in the bi-layered structures. Furthermore, structures showed conduction velocities of 16.9 ± 2.3 cm s^{-1}, with the ability to be paced to 300 ms (3.33 Hz) from 800 ms (1.25 Hz), before being recovered to 800 ms pacing. ADP_{50} and ADP_{80} were noted as 128 ± 12.0 and 186 ± 17.7 ms, respectively.

4. Discussion

Mimicking the myocardium in both form and function has been a goal for researchers in the cardiovascular field for decades. Not only is the heart a cellularly complex organ, but a structurally sophisticated one at that, and mimicking it as a living, electrical, mechanical structure is no easy feat. In this study, a new fabrication method using hiPSC derived cardiac cells for producing engineered cardiac tissue was developed and characterized. This method was based on a bottom-up LbL concept, to allow for enhanced viability and robustness over a 4-week period, as well as the development of physiologically relevant structures on a cellular and microstructure level. This study is the first to our knowledge to show large and easily scalable (1 × 2 cm^2) hiPSC-derived cardiac tissue surrogates that are thick (~1.73 mm), viable and prevascularized without significant neocrosis/apoptosis during 4-weeks following up assessments. Not only have we demonstrated that these structures show minimal necrosis (<5.4%) over a 4 week period, but also that they develop enhanced myocyte maturation as evidenced by characteristics in subcellular structure, electrophysiology, and calcium-handling capabilities. Quantification of the temporal stability of the relative expression of CD31 to cTnT as well as the relative expression of cTnT to DAPI further supported the findings showing minimal necrosis throughout the structures (supplemental figure 4). Additionally, this study quantified the temporal changes that occur during ECM remodeling in the engineered tissue surrogates via immunofluorescent staining, as well as modeling of viscoelastic properties.

Increases in the elastic modulus of engineered cardiac tissue surrogates cultured over 4 weeks were noted, but not as significant as was expected. Significant changes in the viscosity of the engineered tissue surrogates were noted after 2 weeks in culture. Due to the dynamic nature of ECM remodeling, it is difficult to discern which ECM component was mostly responsible for the reduction in viscosity noted in week 2, but general trends suggested reduced laminin could be responsible. Furthermore, the increase in fibronectin expression observed in week 2 coincided with the notable formation of branched vessel-like structures in the cardiac tissue surrogates. As fibronectin is highly expressed in the heart during early stages of embryogenesis and has been shown to be vital in the vasculogenesis process [65] these observations are likely linked. Regulation of vessel formation via an ‘on-off ‘ switch was likely achieved via the expression of Col4 at week 2 [66, 67].

The temporal viscoelastic properties of the engineered tissue surrogates were compared to those of healthy mouse LV tissue. The elasticity moduli reported in this study ranged between ~4.7–5.8 kPa, while the control mouse samples were 6.4 kPa, suggesting that the engineered tissue designed in this study had viscoelastic properties comparable to healthy LV tissue. Comparable elasticity values can be difficult to obtain in the literature due to variations in testing methods; however, healthy rat heart tissue elasticity has been reported to be 18 ± 2 kPa [71], while embryonic mouse epicardial tissue has been reported to have an elastic modulus of 12 ± 4 kPa [72]. Equilibrium moduli values for the bi-layered engineered tissue fell short when compared to healthy mouse LV tissue, though not by a statistically significant amount. This could, in part, be because primary structural ECM deposition was dependent on iCMs alone, whereas native cardiac tissue consists of known structural ECM-producing cells specifically, FBs.

Cardiac cells are under constant, self-generated cyclic mechanical stress, which can affect their differentiation, development as well as maturation. Additional loading of CMs has shown to be an effective tool in advancing certain maturation markers, like the upregulation of connexin-43, in these cells. Stretching has been demonstrated to directly affect the activity of ion channels and increase GJ-mediated cell coupling [73–76]. The bi-layered tissue surrogate developed during this study did not undergo any additional mechanical or electrical loading, yet was still able to develop physiologically relevant ultrastructural attributes like increased sarcomere length and mitochondrial alignment along the contractile elements. The mechanical forces, however faint, that the iCMs cyclically generate, are also a source of constant fluidic motion and convection within the culture environment and may contribute to the system’s ability to remain viable for weeks with minimal cell necrosis. Normal functions of CMs require the ECs in the microenvironment, which likely contribute to the novel fabricated thicker and functional cardiac tissue surrogates in the present study. In addition to the natural motion of the tissue surrogate, the formation of branched vessel-like structures may enhance the oxygen and nutrients delivery to the center of the thicker engineered cardiac tissue.

Cardiac transverse tubules (t-tubules) (figures 9(a) and (b)) are highly branched invaginations of CM sarcolemma that are rich in ion channels essential for excitation-contraction coupling, maintenance of resting membrane potential, action potential initiation and regulation, and signaling transduction. Mature t-tubule networks are present in

mammalian ventricular CMs, with the transverse components of t-tubules occurring near sarcomeric z-discs. Cardiac t-tubules contain membrane microdomains, enriched with ion channels and signaling molecules, and as such, are vital signaling hubs in the regulation of CM function. Dyads formed at the junctions between the t-tubule membrane and neighboring sarcoplasmic reticulum (SR) are vital in calcium signaling and EC coupling necessary for beat-to-beat cardiac contraction. The juxtaposition of the L-type Ca channel located in the t-tubule membrane with the RyR2, the major cardiac SR Ca^{2+} release channel, is necessary for the initiation of the proper calcium transients required following each beat-to-beat action potential. These systems are thought to promote the synchronous activation of the whole depth of the cell despite the fact that the signal to contract is relayed across the external membrane. The importance of the t-tubule network should not be underestimated, as it is responsible for one-third of the capacitance of the membrane, along with most of the influx of Ca^{2+} that triggers the release of intracellular SR Ca^{2+} enters across the t-tubular fraction [77]. Increases in the expression of t-tubule markers like JP2 are indicative of improved calcium handling abilities [78, 79]. Conduction velocities that approach those seen in native LV tissue (30–100 cm s^{-1} [80]) have rarely been achieved in 3D structures with hiPSCs-CMs. Structures consisting of cells from neonatal rats have, however, been shown to reach velocities of up to ~32 cm s^{-1} [81]. The LbL cardiac tissue surrogate produced in the current study (figure 1) does, however, outcompete its predecessors with its 16.9 $\pm$ 2.3 cm s^{-1}, compared to 14.1 $\pm$ 1.0 cm s^{-1} [21]. The ability of the bi-layered structures to be paced to 300 ms without becoming arrhythmogenic was a further indication of their robustness and capability to perform under high-stress conditions [82].

It should be noted that, even though this 3D *In vitro* study was performed over an extended period (4 weeks), it only represents a brief moment in time in terms of the characteristics of a larger ensemble. In order to better understand the system and continue optimization, longer-term culture studies, along with implantation success, have to be assessed. Furthermore, incorporating directional tissue maturation techniques, using a perfusion system as opposed to static culture [83], including electrical or mechanical stimulation [68, 82, 84, 85], could further enhance tissue performance and allow for viscoelastic engineered tissue surrogates that further resembles the native myocardium.

5. Conclusions

Here we have shown how modular fabrication methods, like LbL, can be utilized and optimized to yield thick (~1.73 mm), viable, easy-to-scale-to clinically relevant sized cardiac tissue surrogates. *in vitro* characterization showed tissue structures resembling those of native cardiac tissue, both structurally and functionally. Well-developed calcium-handling machinery, minimal arrhythmogenic potential, and promising conduction velocities were observed. Viscoelastic characterization and comparison with native mouse LV tissue showed that the Generalized Maxwell model of order 4 described the samples very well. The viscoelastic characterization also suggested that the addition of structural ECM producing cells, specifically FBs, may allow for production of cardiac tissue equivalents that further mimic native myocardial tissue.

Future work will focus on the incorporation of additional cells like FBs, yielding further biomimetic structures and allowing for the expansion of potential theranostic applications. *In vivo* studies in a large animal model will also commence in order to assess the potential clinical application of these larger, thicker, cardiac tissue equivalents. Assessment of improvement will include the engraftment rate of transplanted cells, LV dilatation, LV wall stress, infarct size, and arrhythmogenic potential.

Supplementary Material

Refer to Web version on PubMed Central for supplementary material.

Acknowledgments

This study was supported in part by the National Institutes of Health (NIH) through grants NHLBI grants RO1 HL95077, HL114120, HL131017, and HL149137. The authors would like to thank Dr Chengming Fan for surgical assistance, Dr Yanwen Liu for their excellent technical assistance, Dr Silvio Litovsky for cardiac pathology assistance and the UAB High-Resolution Imaging Facility as well as the UAB Pathology Core Lab for their assistance with sample preparation. All mechanical experiments were performed in the UAB Experimental Biomechanics Core (EBC).

References

[1]. Lucas DT and Szweda LI 1999 Declines in mitochondrial respiration during cardiac reperfusion: age-dependent inactivation of α-ketoglutarate dehydrogenase PNAS 96 6689–93 [PubMed: 10359773]

[2]. Lake CL, Sellers TD and Crosby IK 1985 Wellons HA and crampton RS. Effects of coronary grafting technique upon reperfusion cardiac rhythm, ventricular function, and other variables Am. Surg 51 497–503 [PubMed: 3876044]

[3]. Murphy E and Steenbergen C 2008 Mechanisms underlying acute protection from cardiac ischemia-reperfusion injury Physiol Rev. 88 581–609 [PubMed: 18391174]

[4]. Ye L et al. 2014 Cardiac repair in a porcine model of acute myocardial infarction with human induced pluripotent stem cell-derived cardiovascular cells Cell Stem Cell 15 750–61 [PubMed: 25479750]

[5]. Xiaojun L, Cheston H, Gisela W, Kexian Z, Laurie BH, Samira M A, Kunil KR, Jianhua Z, Timothy JK and Sean PP 2012 Robust cardiomyocyte differentiation from human pluripotent stem cells via temporal modulation of canonical Wnt signaling Proc. Natl Acad. Sci. USA 109 E1848–57 [PubMed: 22645348]

[6]. Xiaojun L, Xiaoping B, Abraham - A-A, Jialu L, Yue W, Wentao D, Kaitlin KD, Eric VS and Sean PP 2014 Efficient differentiation of human pluripotent stem cells to endothelial progenitors via small-molecule activation of WNT signaling Stem Cell Rep. 3 804–16

[7]. Ikada Y ed 2006 Chapter 4 Challenges in Tissue Engineering Interface Science and Technology (Amsterdam: Elsevier) 8 pp 423–62

[8]. Rumberger JA 1994 Ventricular dilatation and remodeling after myocardial infarction Mayo Clinic Proc. 69 664–74

[9]. Holmes JW, Borg TK and Covell JW 2005 Structure and mechanics of healing myocardial infarcts Annu. Rev. Biomed. Eng 7 223–53 [PubMed: 16004571]

[10]. Fung YC 1993 Biomechanics: Mechanical Properties of Living Tissues (Berlin: Springer)

[11]. Sacks MS 2001 Biaxial mechanical evaluation of planar biological materials Cardiovascular Soft Tissue Mechanics eds Cowin SC and Humphrey JD (Dordrecht: Springer Netherlands) pp 199–246

[12]. Wang B, Borazjani A, Tahai M, Curry AL, Simionescu DT, Guan J, To F, Elder SH and Liao J 2010 Fabrication of cardiac patch with decellularized porcine myocardial scaffold and bone marrow mononuclear cells J. Biomed. Mater. Res. A 94 1100–10 [PubMed: 20694977]

[13]. Engler AJ, Sen S, Sweeney HL and Discher DE 2006 Matrix elasticity directs stem cell lineage specification Cell 126 677–89 [PubMed: 16923388]

[14]. Reilly GC and Engler AJ 2010 Intrinsic extracellular matrix properties regulate stem cell differentiation J. Biomech 43 55–62 [PubMed: 19800626]

[15]. Freed LE 2006 Advanced tools for tissue engineering: scaffolds, bioreactors, and signaling Tissue Eng. 12 3285–305 [PubMed: 17518670]

[16]. Richardson JJ, Björnmalm M and Caruso F 2015 Technology-driven layer-by-layer assembly of nanofilms Science 348 aaa2491

[17]. Zhang X, Chen H and Zhang H 2007 Layer-by-layer assembly: from conventional to unconventional methods Chem. Commun 14 1395–405

[18]. Kirkland JJ 1965 Porous thin-layer modified glass bead supports for gas liquid chromatography Anal. Chem 37 1458–61

[19]. Jin W, Toutianoush A and Tieke B 2003 Use of polyelectrolyte layer-by-layer assemblies as nanofiltration and reverse osmosis membranes Langmuir 19 2550–3

[20]. Siepmann J and Peppas NA 2000 Hydrophilic matrices for controlled drug delivery: an improved mathematical model to predict the resulting drug release kinetics (the ‘sequential layer’ model) Pharm. Res 17 1290–8 [PubMed: 11145237]

[21]. Gao L et al. 2018 Large cardiac muscle patches engineered from human induced-pluripotent stem cell-derived cardiac cells improve recovery from myocardial infarction in swine Circulation 137 1712–30 [PubMed: 29233823]

[22]. Donath E, Sukhorukov GB, Caruso F, Davis SA and Möhwald H 1998 Novel hollow polymer shells by colloid-templated assembly of polyelectrolytes Angew. Chem., Int. Ed 37 2201–5 10.1002/(SICI)1521-3773(19980904)37:16<2201::AID-ANIE2201>3.0.CO;2-E

[23]. Dreaden EC, Morton SW, Shopsowitz KE, Choi J-H, Deng ZJ, Cho N-J and Hammond PT 2014 Bimodal tumor-targeting from microenvironment responsive hyaluronan layer-by-layer (LbL) nanoparticles ACS Nano 8 8374–82 [PubMed: 25100313]

[24]. Cui J, Liu Y and Hao J 2009 Multiwalled carbon-nanotube-embedded microcapsules and their electrochemical behavior J. Phys. Chem. C 113 3967–72

[25]. Lulevich VV, Andrienko D and Vinogradova OI 2004 Elasticity of polyelectrolyte multilayer microcapsules J. Chem. Phys 120 3822–6 [PubMed: 15268547]

[26]. Best JP, Neubauer MP, Javed S, Dam HH, Fery A and Caruso F 2013 Mechanics of pH-responsive hydrogel capsules Langmuir 29 9814–23 [PubMed: 23886008]

[27]. Rother J, Richter C, Turco L, Knoch F, Mey I, Luther S, Janshoff A, Bodenschatz E and Tarantola M 2015 Crosstalk of cardiomyocytes and fibroblasts in co-cultures Open Biol. 5 150038 [PubMed: 26085516]

[28]. Oliver Cassell CS, Stefan Hofer OP, Morrison WA and Knight KR 2002 Vascularisation of tissue-engineered grafts: the regulation of angiogenesis in reconstructive surgery and in disease states Br. J. Plast. Surg 55 603–10 [PubMed: 12550111]

[29]. Risau W 1997 Mechanisms of angiogenesis Nature 386 671–4 [PubMed: 9109485]

[30]. Ishaug-Riley SL, Crane-Kruger GM, Yaszemski MJ and Mikos AG 1998 Three-dimensional culture of rat calvarial osteoblasts in porous biodegradable polymers Biomaterials 19 1405–12 [PubMed: 9758040]

[31]. Marchionni MA 1995 neu tack on neuregulin Nature 378 334–5 [PubMed: 7477364]

[32]. Lee K-F, Simon H, Chen H, Bates B, Hung M-C and Hauser C 1995 Requirement for neuregulin receptor erbB2 in neural and cardiac development Nature 378 394–8 [PubMed: 7477377]

[33]. Bjarnegård M, Enge M, Norlin J, Gustafsdottir S, Fredriksson S, Abramsson A, Takemoto M, Gustafsson E, Fässler R and Betsholtz C 2004 Endothelium-specific ablation of PDGFB leads to pericyte loss and glomerular, cardiac and placental abnormalities Development 131 1847–57 [PubMed: 15084468]

[34]. Gödecke A, Heinicke T, Kamkin A, Kiseleva I, Strasser RH, Decking UKM, Stumpe T, Isenberg G and Schrader J 2001 Inotropic response to β-adrenergic receptor stimulation and anti-adrenergic effect of ACh in endothelial NO synthase-deficient mouse hearts J. Physiol 532 195–204 [PubMed: 11368026]

[35]. Champion HC, Georgakopoulos D, Takimoto E, Isoda T, Wang Y and Kass DA 2004 Modulation of in vivo cardiac function by myocyte-specific nitric oxide synthase-3 Circ. Res 94 657–63 [PubMed: 14752030]

[36]. Barouch LA et al. 2002 Nitric oxide regulates the heart by spatial confinement of nitric oxide synthase isoforms Nature 416 337–9 [PubMed: 11907582]

[37]. Dunn KK, Reichardt IM, Simmons AD, Jin G, Floy ME, Hoon KM and Palecek SP 2019 Coculture of endothelial cells with human pluripotent stem cell-derived cardiac progenitors reveals a differentiation stage-specific enhancement of cardiomyocyte maturation Biotechnol. J 14 1800725

[38]. Khademhosseini A, Suh KY, Yang JM, Eng G, Yeh J, Levenberg S and Langer R 2004 Layer-by-layer deposition of hyaluronic acid and poly-l-lysine for patterned cell co-cultures Biomaterials 25 3583–92 [PubMed: 15020132]

[39]. Ware BR, Durham MJ, Monckton CP and Khetani SR 2018 A cell culture platform to maintain long-term phenotype of primary human hepatocytes and endothelial cells Cell. Mol. Gastroenterol. Hepatol 5 187–207 [PubMed: 29379855]

[40]. Sasaki K et al. 2017 Construction of three-dimensional vascularized functional human liver tissue using a layer-by-layer cell coating technique Biomaterials 133 263–74 [PubMed: 28448819]

[41]. Norotte C, Marga FS, Niklason LE and Forgacs G 2009 Scaffold-free vascular tissue engineering using bioprinting Biomaterials 30 5910–7 [PubMed: 19664819]

[42]. Bursac N, Papadaki M, Cohen RJ, Schoen FJ, Eisenberg SR, Carrier R, Vunjak-Novakovic G and Freed LE 1999 Cardiac muscle tissue engineering: toward an In vitro model for electrophysiological studies Am. J. Physiol. Heart. Circ. Physiol 277 H433–H444

[43]. Shadrin IY, Allen BW, Qian Y, Jackman CP, Carlson AL, Juhas ME and Bursac N 2017 Cardiopatch platform enables maturation and scale-up of human pluripotent stem cell-derived engineered heart tissues Nat. Commun 8 1825 [PubMed: 29184059]

[44]. Shimizu T, Yamato M, Kikuchi A and Okano T 2001 Two-dimensional manipulation of cardiac myocyte sheets utilizing temperature-responsive culture dishes augments the pulsatile amplitude Tissue Eng. 7 141–51 [PubMed: 11304450]

[45]. Munro ML, Jayasinghe ID, Wang Q, Quick A, Wang W, Baddeley D, Wehrens XHT and Soeller C 2016 Junctophilin-2 in the nanoscale organisation and functional signalling of ryanodine receptor clusters in cardiomyocytes Journal of Cell Science 129 4388–98 [PubMed: 27802169]

[46]. Landstrom AP, Kellen CA, Dixit SS, RJv O, Garbino A, Weisleder N, Ma J, Wehrens XHT and Ackerman MJ 2011 Junctophilin-2 expression silencing causes cardiocyte hypertrophy and abnormal intracellular calcium-handling Circulation: Heart Failure 4 214–23 [PubMed: 21216834]

[47]. Burridge PW et al. 2014 Chemically defined generation of human cardiomyocytes Nat Methods 11 855–60 [PubMed: 24930130]

[48]. Lian X, Zhang J, Azarin SM, Zhu K, Hazeltine LB, Bao X, Hsiao C, Kamp TJ and Palecek SP 2012 Directed cardiomyocyte differentiation from human pluripotent stem cells by modulating Wnt/β-catenin signaling under fully defined conditions Nat. Protoc 8 162 [PubMed: 23257984]

[49]. Zhu W, Gao L and Zhang J 2017 Pluripotent stem cell derived cardiac cells for myocardial repair JoVE e55142

[50]. Su L et al. 2018 The prostaglandin H2 analog U-46619 improves the differentiation efficiency of human induced pluripotent stem cells into endothelial cells by activating both p38MAPK and ERK1/2 signaling pathways Stem Cell Res. Ther 9 313 [PubMed: 30442193]

[51]. Zhang S, Dutton JR, Su L, Zhang J and Ye L 2014 The influence of a spatiotemporal 3D environment on endothelial cell differentiation of human induced pluripotent stem cells Biomaterials 35 3786–93 [PubMed: 24485793]

[52]. Li W, Germain RN and Gerner MY 2019 High-dimensional cell-level analysis of tissues with Ce3D multiplex volume imaging Nat. Protoc 14 1708–33 [PubMed: 31028373]

[53]. Pollack GH 1970 Maximum velocity as an index of contractility in cardiac muscle Circulation Research 26 111–27 [PubMed: 5410091]

[54]. Ramadan S, Paul N and Naguib HE 2017 Standardized static and dynamic evaluation of myocardial tissue properties Biomed. Mater. (Bristol, England) 12 025013

[55]. Pollard AE and Barr RC 2013 A new approach for resolution of complex tissue impedance spectra in hearts IEEE Trans. Biomed. Eng 60 2494–503 [PubMed: 23625349]

[56]. Waits CMK, Barr RC and Pollard AE 2014 Sensor spacing affects the tissue impedance spectra of rabbit ventricular epicardium Am. J. Physiol. Heart Circ. Physiol 306 H1660–H1668 [PubMed: 24778170]

[57]. Sowell B and Fast VG 2012 Ionic mechanism of shock-induced arrhythmias: role of intracellular calcium Heart Rhythm 9 96–104 [PubMed: 21878203]

[58]. Linkermann A, Kunzendorf U and Krautwald S 2014 Phosphorylated MLKL causes plasma membrane rupture Mol. Cell Oncol 1 e29915–e29915 [PubMed: 27308322]

[59]. Negroni A, Colantoni E, Pierdomenico M, Palone F, Costanzo M, Oliva S, Tiberti A, Cucchiara S and Stronati L 2017 RIP3 AND pMLKL promote necroptosis-induced inflammation and alter membrane permeability in intestinal epithelial cells Digestive Liver Dis. 49 1201–10

[60]. Wendel JS, Ye L, Tao R, Zhang J, Zhang J, Kamp TJ and Tranquillo RT 2015 Functional effects of a tissue-engineered cardiac patch from human induced pluripotent stem cell-derived cardiomyocytes in a rat infarct model Stem Cells Transl. Med 4 1324–32 [PubMed: 26371342]

[61]. Bax NAM, van Marion MH, Shah B, Goumans M-J, Bouten CVC and D W J V D S 2012 Matrix production and remodeling capacity of cardiomyocyte progenitor cells during In vitro differentiation J. Mol. Cell. Cardiol 53 497–508 [PubMed: 22820459]

[62]. Lu P, Takai K, Weaver VM and Werb Z 2011 Extracellular matrix degradation and remodeling in development and disease Cold Spring Harbor Perspect. Biol 3 a005058

[63]. Ford AJ and Rajagopalan P 2018 Extracellular matrix remodeling in 3D: implications in tissue homeostasis and disease progression Wiley Interdiscip Rev Nanomed Nanobiotechnol 10 e1503 [PubMed: 29171177]

[64]. Cox TR and Erler JT 2011 Remodeling and homeostasis of the extracellular matrix: implications for fibrotic diseases and cancer Dis. Model Mech. 4 165–78 [PubMed: 21324931]

[65]. George EL, E N G-L, R S P-K, Rayburn H andHynes RO 1993 Defects in mesoderm, neural tube and vascular development in mouse embryos lacking fibronectin Development (Cambridge, England) 119 1079–91

[66]. Carmeliet P 2003 Angiogenesis in health and disease Nat. Med 9 653–60 [PubMed: 12778163]

[67]. Colorado PC et al. 2000 Anti-angiogenic cues from vascular basement membrane collagen Cancer Res. 60 2520–6 [PubMed: 10811134]

[68]. Ronaldson-Bouchard K, Ma SP, Yeager K, Chen T, Song L, Sirabella D, Morikawa K, Teles D, Yazawa M and Vunjak-Novakovic G 2018 Advanced maturation of human cardiac tissue grown from pluripotent stem cells Nature 556 239–43 [PubMed: 29618819]

[69]. Sheldon CA, Friedman WF and Sybers HD 1976 Scanning electron microscopy of fetal and neonatal lamb cardiac cells J. Mol. Cell. Cardiol 8 853–62 [PubMed: 1003491]

[70]. Anversa P, Olivetti G and Loud AV 1980 Morphometric study of early postnatal development in the left and right ventricular myocardium of the rat. I. Hypertrophy, hyperplasia, and binucleation of myocytes Circulation Research 46 495–502 [PubMed: 6444554]

[71]. Berry MF, Engler AJ, Woo YJ, Pirolli TJ, Bish LT, Jayasankar V, Morine KJ, Gardner TJ, Discher DE and Sweeney HL 2006 Mesenchymal stem cell injection after myocardial infarction improves myocardial compliance Am J Physiol Heart Circ Physiol. 290 H2196–H2203 [PubMed: 16473959]

[72]. Jacot JG, Martin JC and Hunt DL 2010 Mechanobiology of cardiomyocyte development J. Biomech 43 93–8 [PubMed: 19819458]

[73]. Kaushik G and Engler AJ 2014 From stem cells to cardiomyocytes: the role of forces in cardiac maturation, aging, and disease Prog. Mol. Biol. Transl. Sci 126 219–42 [PubMed: 25081620]

[74]. Zhuang J, Yamada KA, Saffitz JE and Kléber AG 2000 Pulsatile stretch remodels cell-to-cell communication in cultured myocytes Circulation Research 87 316–22 [PubMed: 10948066]

[75]. Yamada K, Green KG, Samarel AM and Saffitz JE 2005 Distinct pathways regulate expression of cardiac electrical and mechanical junction proteins in response to stretch Circ. Res 97 346–53 [PubMed: 16037569]

[76]. Wang TL, Tseng YZ and Chang H 2000 Regulation of connexin 43 gene expression by cyclical mechanical stretch in neonatal rat cardiomyocytes Biochem. Biophys. Res. Commun 267 551–7 [PubMed: 10631100]

[77]. Scriven DRL, Dan P and Moore EDW 2000 Distribution of proteins implicated in excitation-contraction coupling in rat ventricular myocytes Biophys. J 79 2682–91 [PubMed: 11053140]

[78]. Parikh SS et al. 2017 Thyroid and glucocorticoid hormones promote functional T-tubule development in human-induced pluripotent stem cell-derived cardiomyocytes Circ. Res 121 1323–30 [PubMed: 28974554]

[79]. Li S, Chen G and Li RA 2013 Calcium signalling of human pluripotent stem cell-derived cardiomyocytes J Physiol 591 5279–90 [PubMed: 24018947]

[80]. Yang X, Pabon L and Murry CE 2014 Engineering adolescence: Maturation of Human Pluripotent Stem Cell–Derived Cardiomyocytes Circulation Research 114 511–23 [PubMed: 24481842]

[81]. Jackman CP, Ganapathi AM, Asfour H, Qian Y, Allen BW, Li Y and Bursac N 2018 Engineered cardiac tissue patch maintains structural and electrical properties after epicardial implantation Biomaterials 159 48–58 [PubMed: 29309993]

[82]. LaBarge W, Mattappally S, Kannappan R, Fast VG, Pretorius D, Berry JL and Zhang J 2019 Maturation of three-dimensional, hiPSC-derived cardiomyocyte spheroids utilizing cyclic, uniaxial stretch and electrical stimulation PloS One 14 e0219442–e0219442 [PubMed: 31276558]

[83]. Zhao F, Pathi P, Grayson W, Xing Q, Locke BR and Ma T 2005 Effects of oxygen transport on 3-D human mesenchymal stem cell metabolic activity in perfusion and static cultures: experiments and mathematical model Biotechnol Prog. 21 1269–80 [PubMed: 16080711]

[84]. Radisic M, Park H, Shing H, Consi T, Schoen FJ, Langer R, Freed LE and Vunjak-Novakovic G 2004 Functional assembly of engineered myocardium by electrical stimulation of cardiac myocytes cultured on scaffolds PNAS 101 18129–34 [PubMed: 15604141]

[85]. Ruan JL, Tulloch NL, Razumova MV, Saiget M, Muskheli V, Pabon L, Reinecke H, Regnier M and Murry CE 2016 Mechanical stress conditioning and electrical stimulation promote contractility and force maturation of induced pluripotent stem cell-derived human cardiac tissue Circulation 134 1557–67 [PubMed: 27737958]

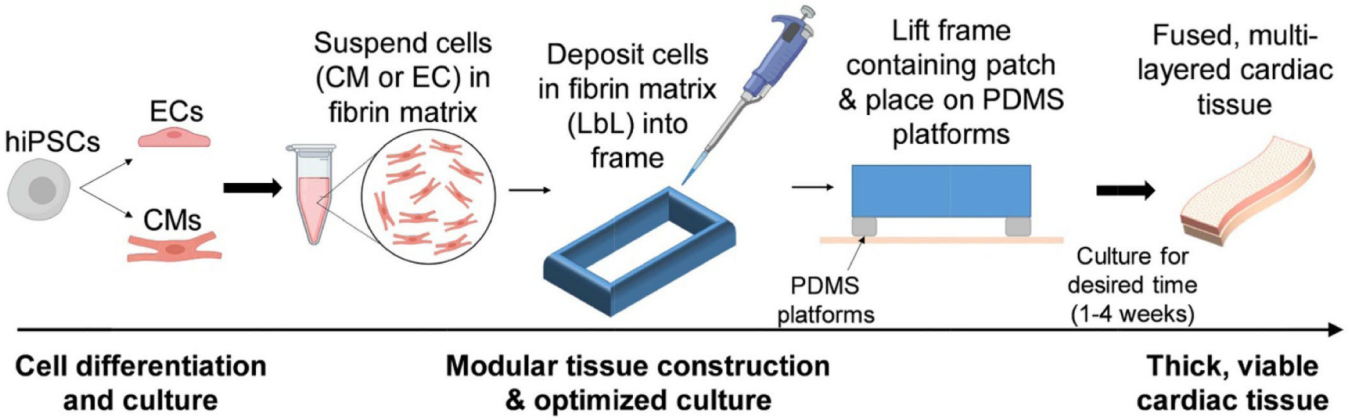

Figure 1.

Basic description of optimized cardiac tissue surrogate fabrication process, allowing for extended culturing of thick tissue structures. The first layer of cells is deposited and cultured for 48 h, after which the second layer is deposited using LbL approach. The second layer of cells is deposited, allowed to polymerize, and the entire structure contained in its frame is then lifted off of the dish surface and placed ontop of PDMS platforms. Thick, viable, multi-layered tissue can be cultured for the desired amount of time (1–4 weeks).

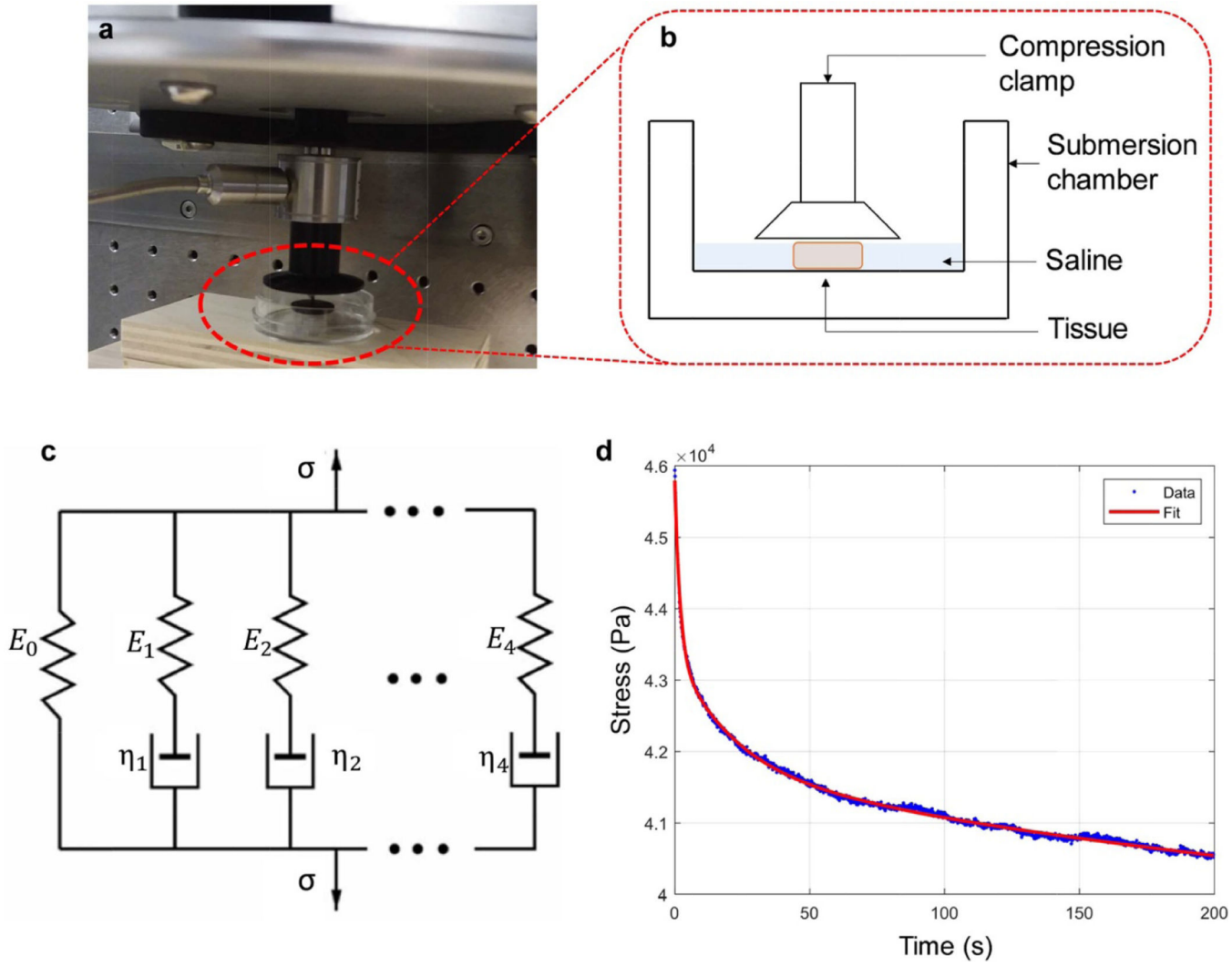

Figure 2.

Shown here is the experimental setup used to quantify the viscoelastic properties of the engineered cardiac tissue. (a) Shows an image of the compression clamp and the submersion chamber, whereas (b) shows a schematic of the experimental setup. (c) Generalized Maxwell model of order 4 schematic. E_i and η_i represent the modulus and viscosity of the i^{th} elements, and σ is the measured stress, with (d) showing the stress relaxation response ('Data') and modeling ('Fit') of PDMS crosslinked at an elastomer:curing agent ratio of 34:1, showing the goodness-of-fit for the generalized Maxwell model of order 4 ($R^2 > 0.98$).

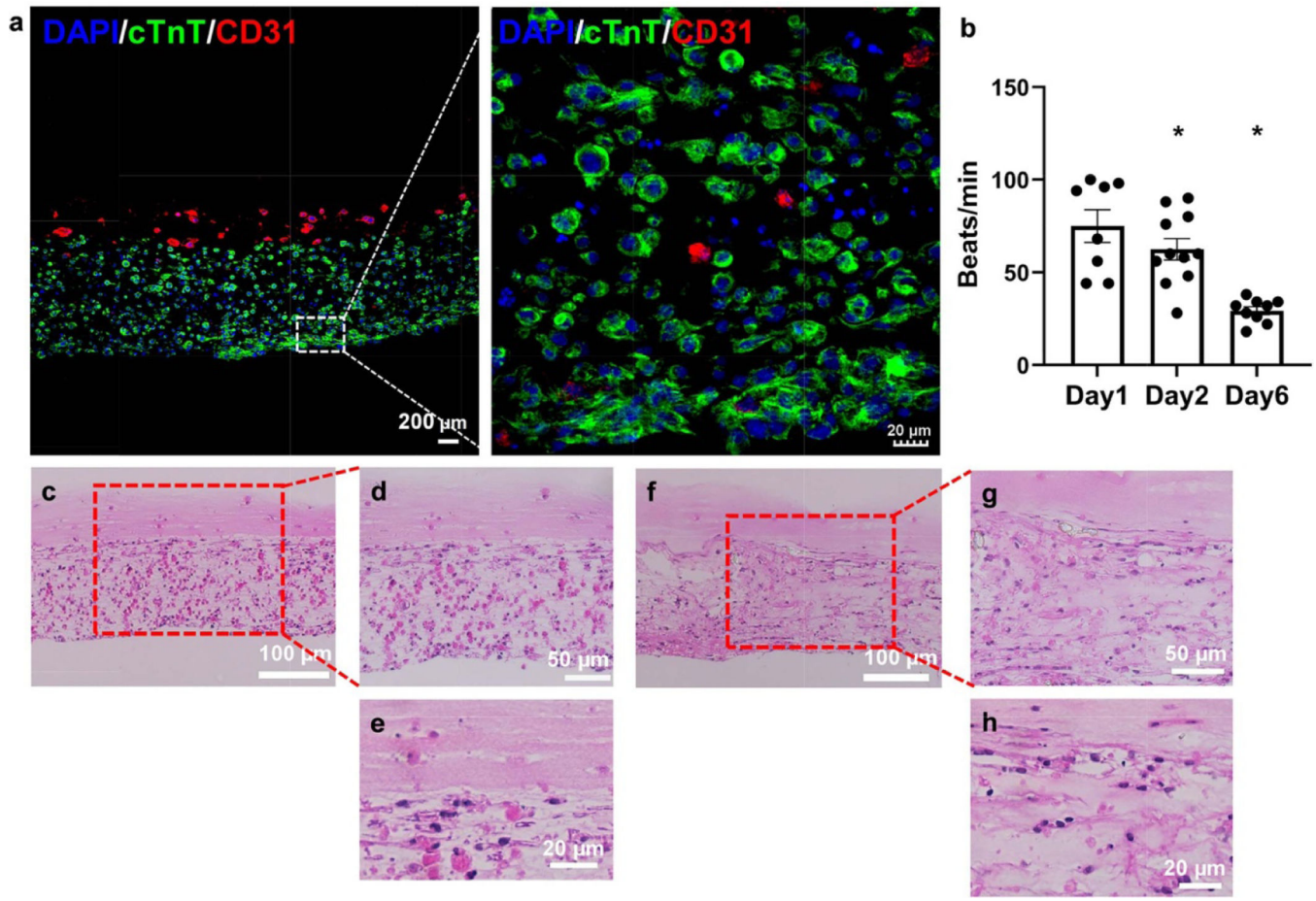

Figure 3.

(a) Confocal micrograph of fabricated LbL cardiac tissue surrogates showing cell distribution and tissue surrogates thickness after 1 week in culture (n = 4). (b) LBL tissue surrogates beat-rate over the first 6 d during culture, $p < 0.05$, (n = 11). H&E staining of LbL tissue surrogates at Day 7 (c)–(e), and Day 28 (f)–(h) of culturing.

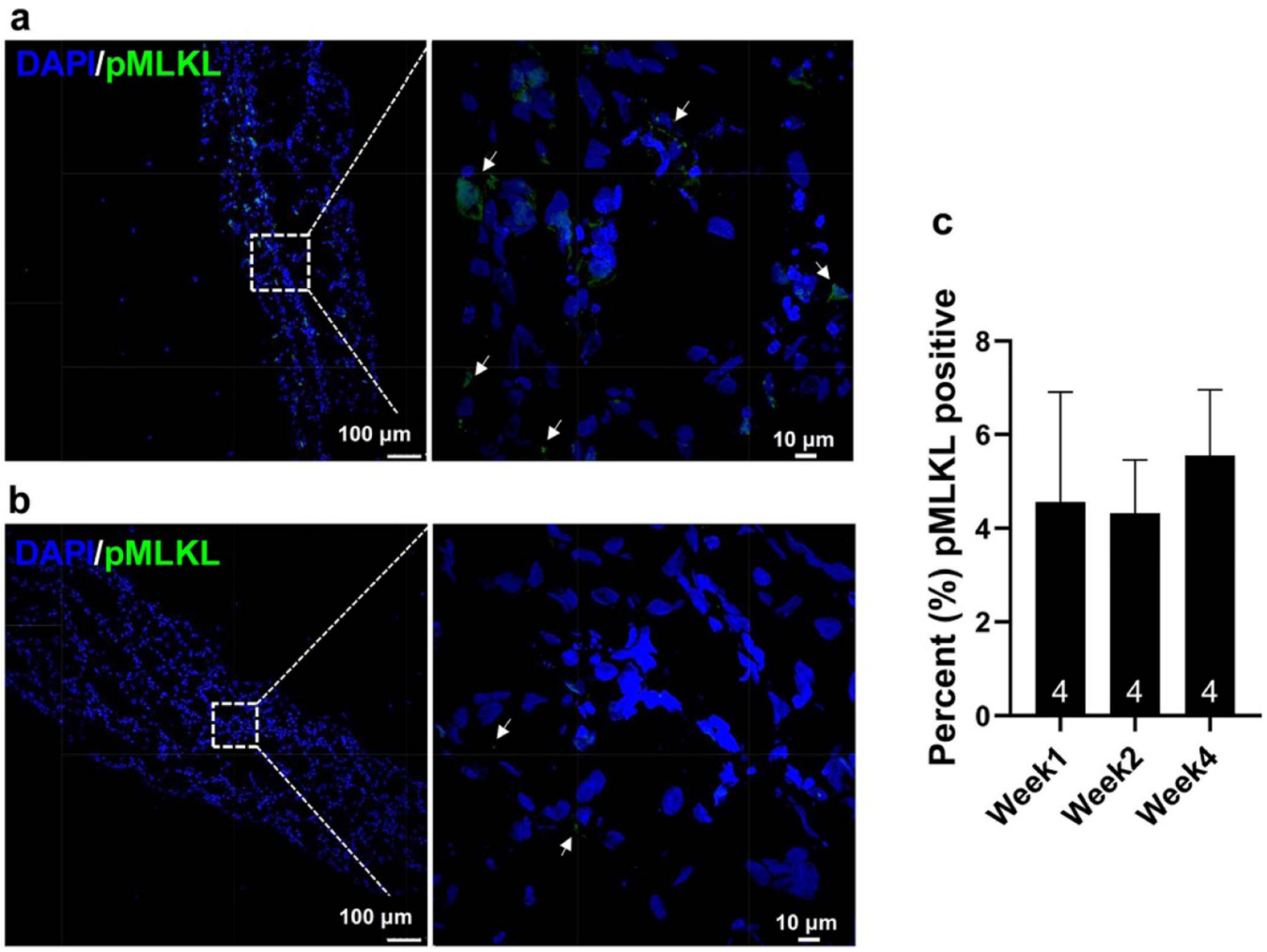

Figure 4.

Confocal micrograph of LbL tissue surrogates displaying necrotic cells identified by the necrosis marker phosphorylated MLKL (Ser358, pMLKL) at week 1 (a) and week 2 (b) of culture. (c) Percentage of necrotic cells in LbL tissue surrogates, (n = 4).

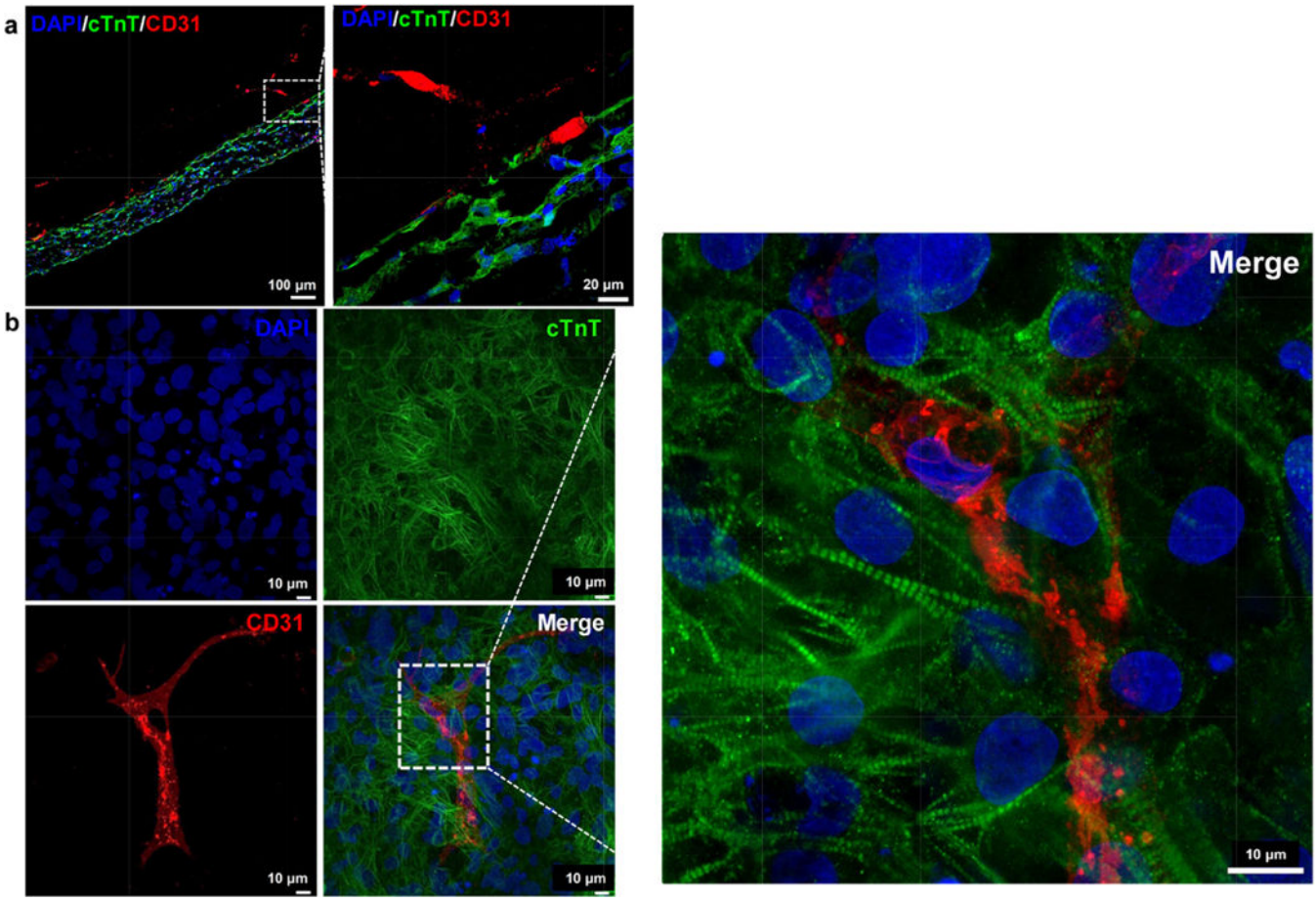

Figure 5.

Fluorescent staining with cTnT and CD31 showing developing vasculature in tissue cultured for (a) 4 weeks, along with (b) whole-mount staining of a 2-week tissue surrogate. Scale bars for the zoomed-in images are 20 μm and 10 μm for (a) and (c) respectively.

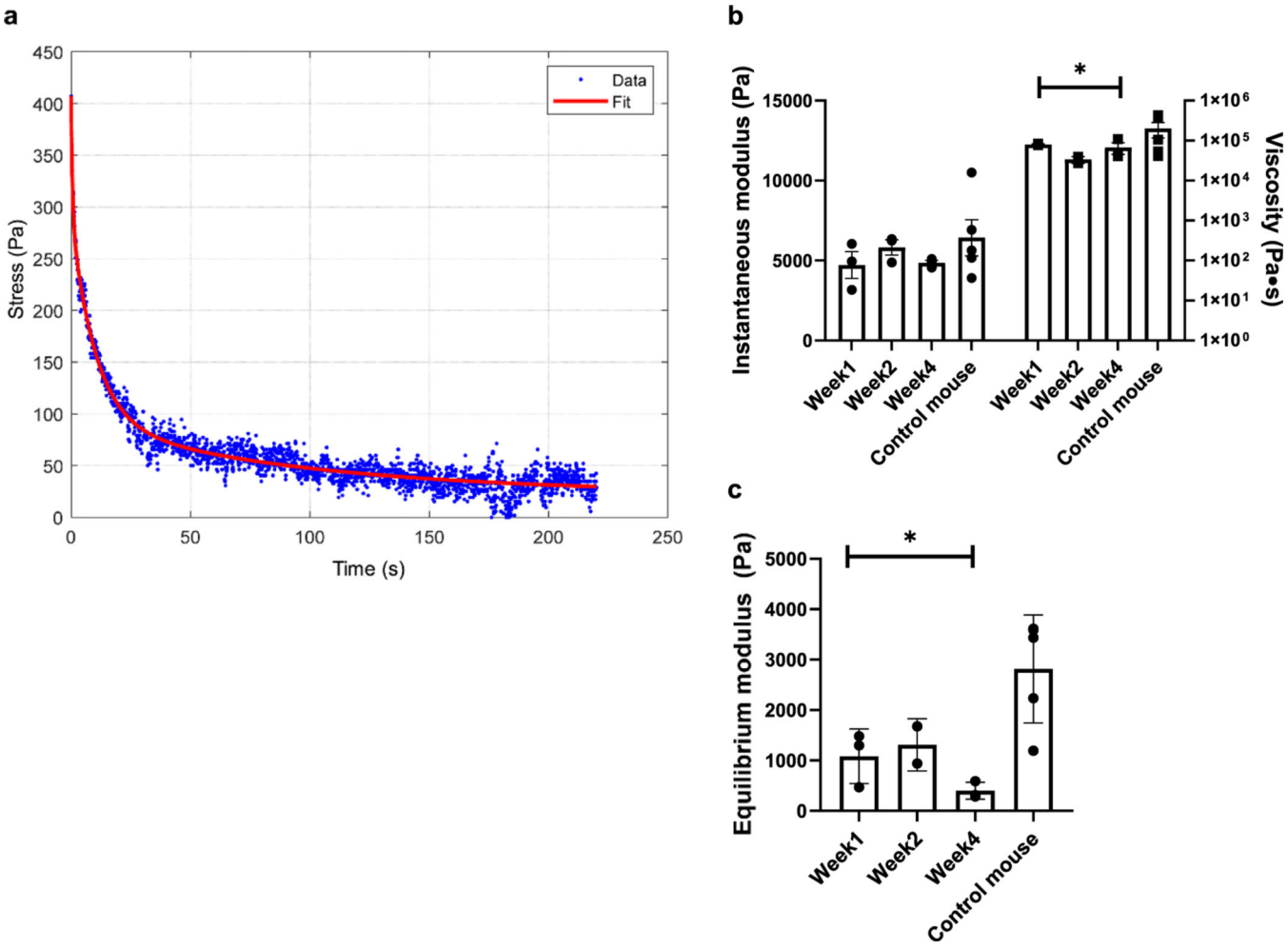

Figure 6:

(a) Stress relaxation response ('Data') and modeling ('Fit') of a 4-week tissue surrogate as well as (b, c) the quantification of the modeling results for all samples over 4 weeks (n = 3 for all groups of tissue surrogates; n = 5 for control mice; $^{*}p < 0.05$).

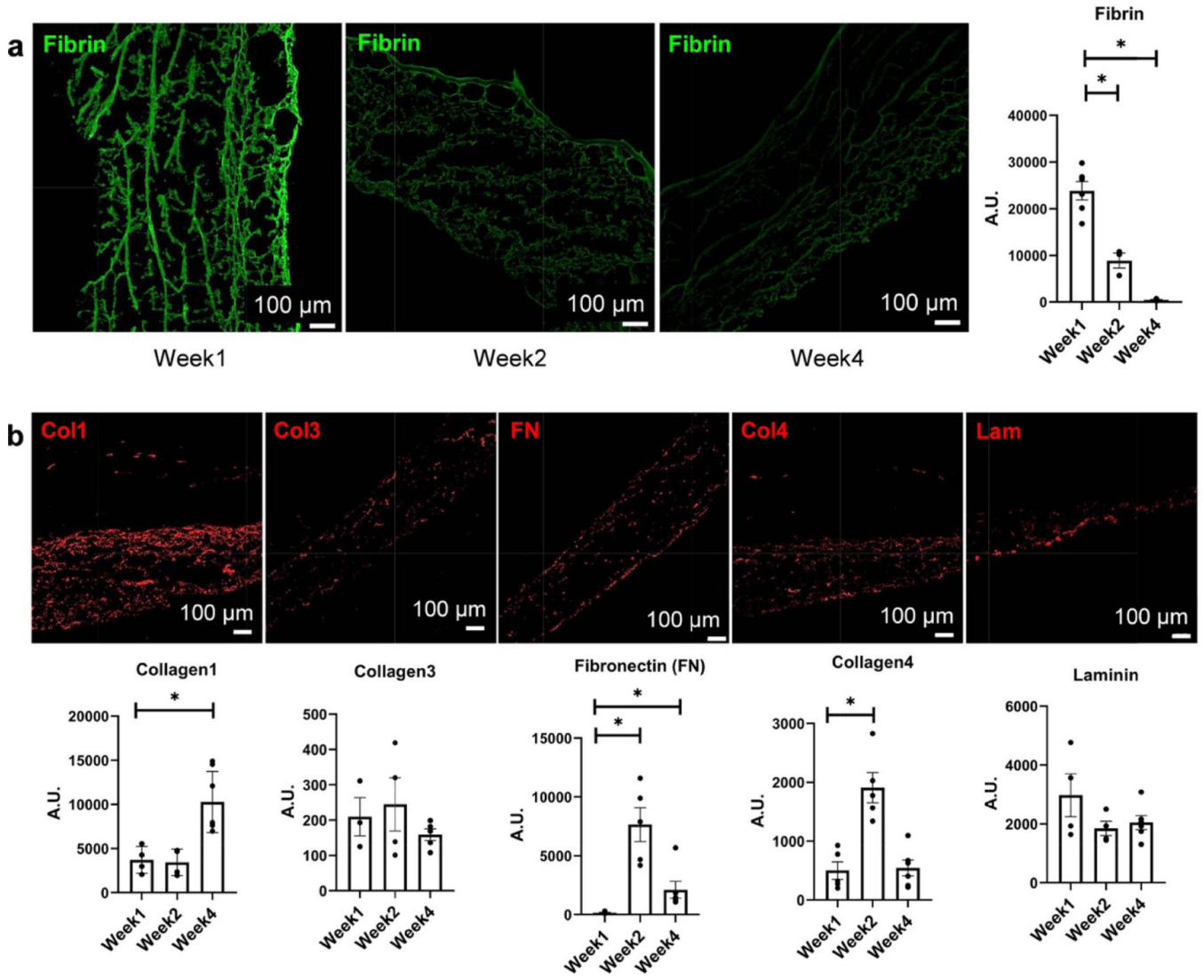

Figure 7.

Representative images and subsequent quantification of ECM evolution over a 4-week period, with (a) showing the degradation of fibrin and (b) showing the deposition of Collagen 1, Collagen 3, Fibronectin (FN), Collagen 4 and Laminin at week 4. Scale bars = 100 µm, n = 5, $^{*}p < 0.05$.

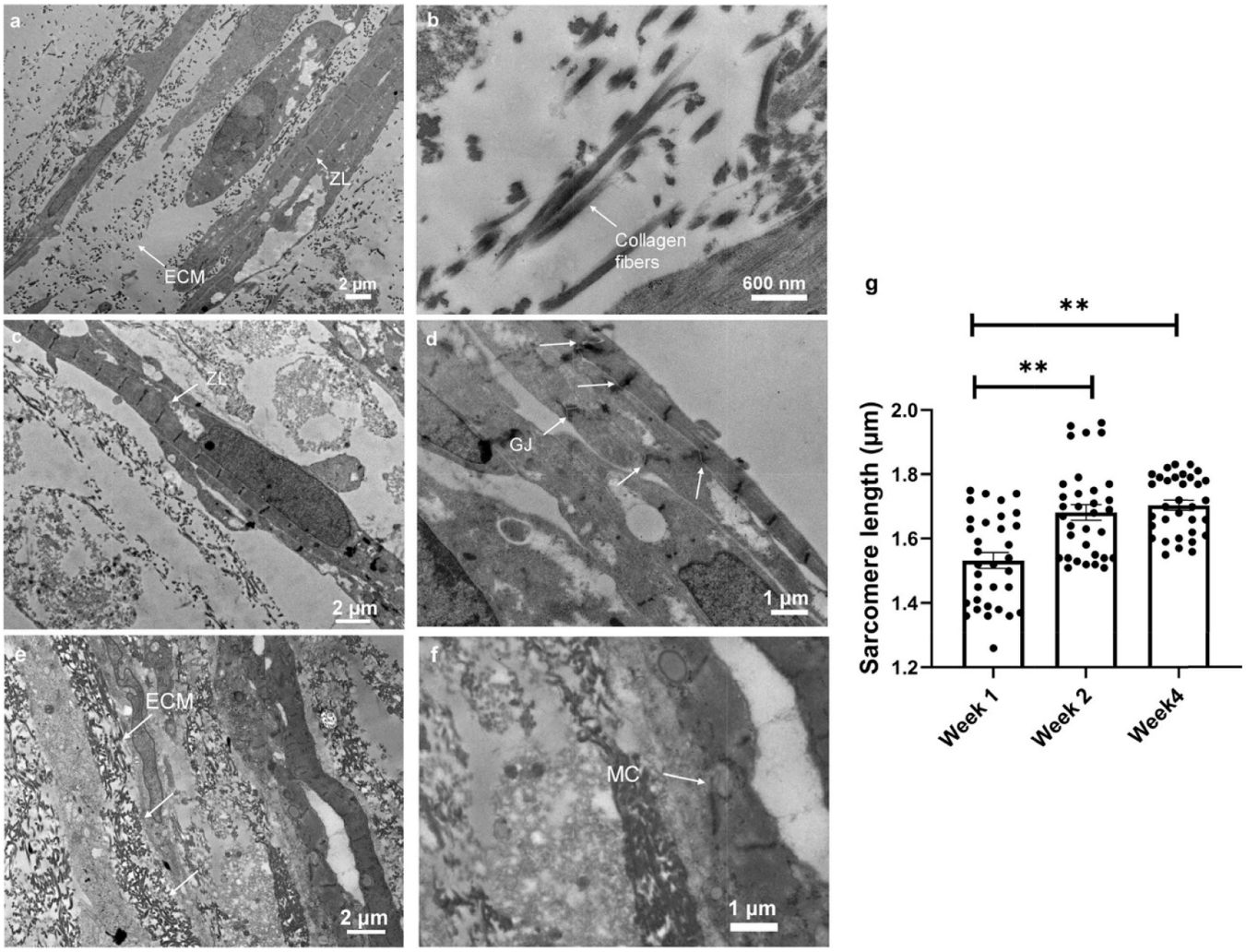

Figure 8.

TEM of bi-layered tissue surrogate (a) 1 week after fabrication, showing alterations in ECM composition as well as cardiomyocyte Z-lines (ZL); (b) higher magnification with collagen fibers clearly distinguishable from other ECM components; (c) 2 weeks after fabrication, showing more distinct Z-lines as well as (d) higher magnification with gap junctions (GJ) between cells; (e) 4 weeks after fabrication, showing further alterations in ECM deposition, as well as (f) higher magnification with mitochondria (MC) starting to arrange along the contractile elements. (g) Sarcomere length comparison (n = 33) between structures cultured for 1 week, 2 weeks and 4 weeks; $^{**}p < 0.0001$.

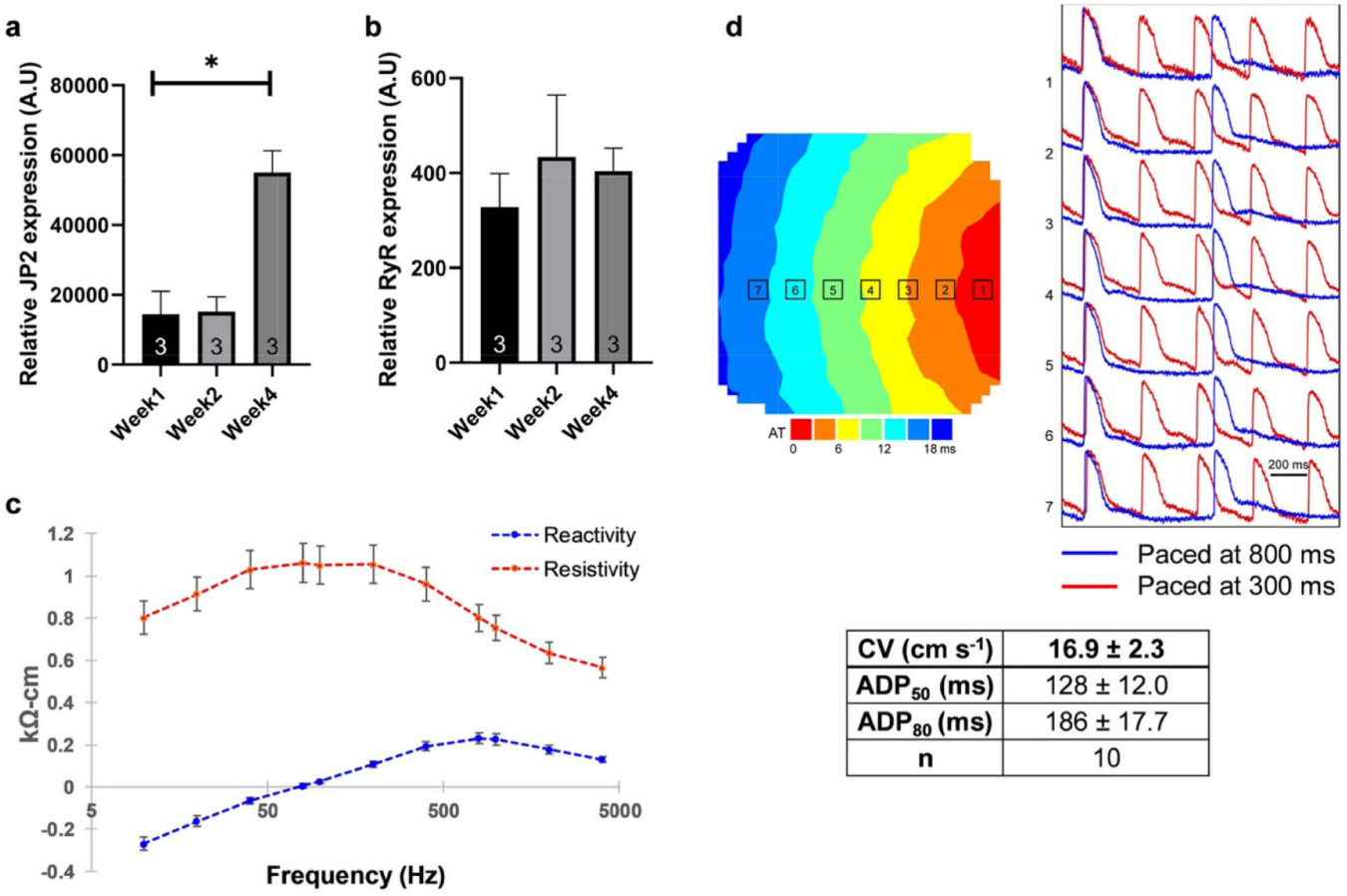

CV (cm s^{-1})	16.9 ± 2.3
ADP_{50} (ms)	128 ± 12.0
ADP_{80} (ms)	186 ± 17.7
n	10

Figure 9.

Expression of (a) JP2 and (b) RyR in the cardiac tissue surrogate structures over the different culture periods, $^{*}p < 0.05$ (n = 3). (c) Tissue reactivity and resistivity shown as a function of stimulation frequency, (n = 15). (d) Summary of tissue optical mapping, with representative signal propagation heatmap as well as pacing at both 300 ms (red) and 800 ms (blue) (n = 10).